Time-Dependent Density Functional Theory Modeling of Spin-Orbit Coupling in Ruthenium and Osmium Solar Cell Sensitizers

3 AUTHORS, INCLUDING:

Enrico Ronca
Princeton University
16 PUBLICATIONS   **386** CITATIONS

Filippo De Angelis
Università degli Studi di Perugia
265 PUBLICATIONS   **11,207** CITATIONS

Time-Dependent Density Functional Theory Modeling of Spin−Orbit Coupling in Ruthenium and Osmium Solar Cell Sensitizers

Enrico Ronca,[†,‡] Filippo De Angelis,[†] and Simona Fantacci*,[†]

[†]Istituto CNR di Scienze e Tecnologie Molecolari (CNR-ISTM), Computational Laboratory for Hybrid/Organic Photovoltaics (CLHYO), via Elce di Sotto 8, I-06123 Perugia, Italy

[‡]Dipartimento di Chimica, Università degli Studi di Perugia, via Elce di Sotto 8, I-06123 Perugia, Italy

S Supporting Information

ABSTRACT: We report on the relevance of spin−orbit coupling on the optical properties of Ru(II)- and Os(II)-polypyridyl dyes effectively employed in dye-sensitized solar cells (DSCs). We include relativistic effects on time-dependent density functional theory calculations of selected complexes by using different levels of calculations, i.e., the scalar zero-order regular approximation (ZORA) and the fully relativistic ZORA including spin−orbit coupling, in such a way so as to disentangle and evaluate the spin−orbit effect. The widely investigated $[M(bpy)_3]^{2+}$ (M = Ru(II) and Os(II)) have been selected as benchmark complexes in our calculations; this is followed by investigation of "realistic" dyes used in DSCs, such as the prototypical N3 dye, its Os-based analogue, and a panchromatic Os(II) dye. We find that in Ru(II) complexes, spin−orbit coupling leads to a slight correction of the spectral shape, whereas only when we include the spin−orbit coupling we are able to reproduce the low-energy absorption bands characteristic of the Os(II) complexes. This study allows us to find a quantitative correlation between the strength of spin−orbit coupling and the metal center, highlighting the secondary effect of the different ligands experienced by the metal center.
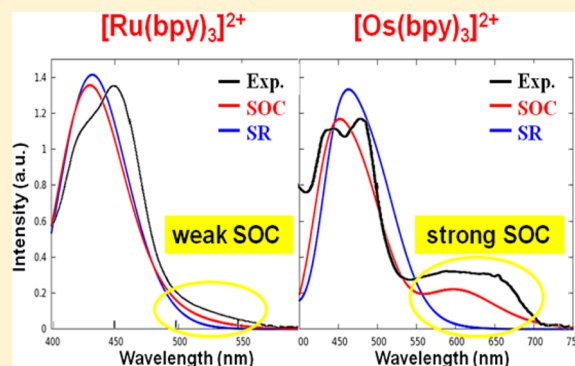
1. INTRODUCTION

Dye-sensitized solar cells (DSCs) represent a low-cost alternative to traditional photovoltaic technology in converting solar light into electricity.[1,2] The efficiency of a DSC is the result of different experimentally accessible parameters, of which the most relevant are the V_{OC}, the voltage at open circuit, and J_{SC}, the short circuit photocurrent density. The V_{OC} is the difference between the quasi-Fermi level of electrons in the semiconductor and the redox potential of the redox shuttle. J_{SC} is related to the monochromatic incident photon-to-current-conversion efficiency (IPCE), which in turn depends on the light harvesting and charge collection efficiency. The maximization of the DSC efficiency involves the optimization of the single components and of the processes underlying the functioning of the device. The dye sensitizer is one of the key DSC components, and many efforts have been made to properly design new organic and metallorganic dyes which entail higher DSC efficiency. Metal−organic dyes hold the record efficiency in DSC applications, having reached an overall power conversion efficiency of over 11% with Ru(II)-polypyridyl complexes[3] and more recently over 12−13% with Zn-porphyrin complexes.[4] The "perfect" sensitizer should possess several main requirements: the presence of an anchoring group which ensures a strong adsorption on the semiconductor oxide surface, high thermal and chemical stability, and a broad and intense absorption in the visible

region of the solar spectrum. One of the challenges in the research of new dyes is harvesting the majority of the available photons, extending the absorption also to the near-infrared (NIR) region. Only a few examples of dyes have been reported that address this requirement.[5−13] Harvesting NIR photons has been barely successful with Ru-based dyes; the replacement of Ru by Os has been exploited to absorb in the NIR region,[14] obtaining promising efficiencies which in turn opened the way to a new generation of solar cell sensitizers.[5,8,15] Interest in panchromatic Ru(II) dyes has been renewed because they cover almost the entire visible light spectrum, with respect to traditional polypyridyl Ru sensitizers, i.e., N719.[3] [Ru(tctpy)(SCN)₃]⁺ (N749) is considered to be the pioneering panchromatic Ru-based dye, known as black dye (hereafter BD).[6,16−18] The BD continues to catalyze interest also for the achieved DSC high efficiency, over 11%, which was recently certified.[19] Various panchromatic Ru(II) sensitizers have been tested in DSCs based on ligand engineering, such as quaterpyridine ligands enforcing a *trans* arrangement of the NCS ancillary groups.[7] Alternatively, the terpyridine ligand was

Scheme 1. Molecular Structures of $[M(bpy)_3]^{2+}$ and $[M(dcbpy)_2(SCN)_2]^{4-}$ (M = Ru, Os) and of $[Os(dcpby)_2(acac)]^{3-}$
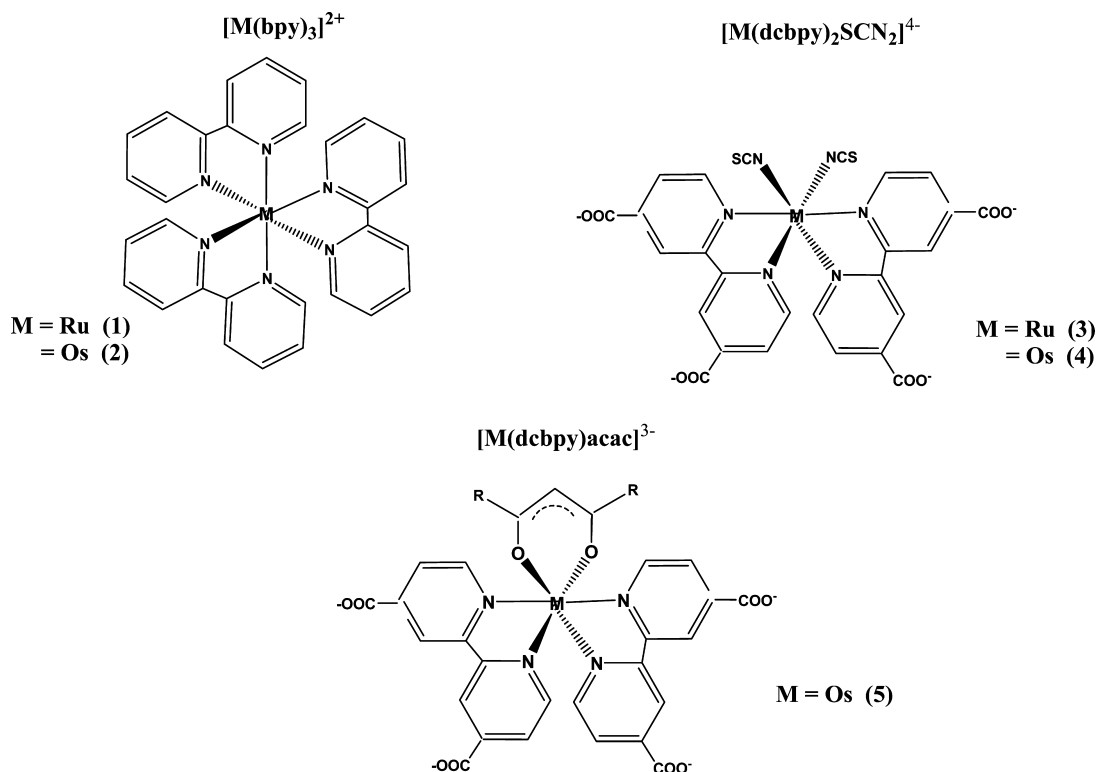
maintained but the three SCN ligands were substituted by Cl and by functionalized bipyridyl ligand.[8] Very recently, Segawa and co-workers proposed an efficient Ru(II)-terpyridyl dye sensitizer, with two chlorine and one -P$(OCH_3)_2(C_6H_6)$ ligand, labeled DX1, which was found to harvest more near -IR light than the BD in the 750−900 nm region.[11] For this dye a crucial role of the singlet−triplet states has been invoked to explain the low-energy absorption with respect to the BD.

Despite the large number of experimental studies reporting on panchromatic and NIR-absorbing dyes, only a few theoretical investigations have been devoted to these sensitizers.[7,20−24] Density functional theory (DFT) and its time-dependent extension (TDDFT) are powerful tools repeatedly employed to understand the electronic and optical properties of realistic dyes used in DSCs.[3,7,20−23,25−31] In combination with efficient algorithms and parallel computers, DFT/TDDFT methods have allowed the simulation of large portions of optical spectra by accurately computing a large number of dye singlet−singlet transitions at reasonable computational costs and also the simulation of the excited states of dye-sensitized TiO_2 models.[32−36]

The calculation of the singlet−triplet oscillator strengths, being entirely originated by spin−orbit coupling, is still not a common procedure. In fact, many quantum chemical codes do not implement spin−orbit coupling within TDDFT; therefore, singlet−triplet excitations are calculated with zero oscillator strength. For the simulation of organic dye spectra, this issue is not relevant because singlet−singlet transitions are responsible for the UV−vis absorption bands. In the case of metal−organic dyes, singlet−triplet transitions might have a central role depending on the nature of the metal. In fact, for heavy metals, singlet triplets strongly couple, thus affecting the optical properties of the complexes;[37] the strength of the spin−orbit coupling influences the intersystem crossing processes and

makes possible the population of triplet states that are otherwise spin-forbidden.[38]

A fully relativistic solution of the 4-component Dirac−Kohn−Sham (DKS) equations is extremely computationally expensive,[39] and its use for the simulation of realistic systems is far from applicable. In this regard, several methods have been developed to solve this equation in an approximated way.[40−44] One of the most successful and accurate strategies used to treat relativistic effects in large molecules is based on the solution of the DKS equation under the 2-component zero-order regular approximation (ZORA). This procedure is able to disentangle the scalar relativistic effects (SR)[41] from the corrections associated with the inclusion of the spin−orbit coupling (SOC) operator.[42,43] Notably, the scalar and spin−orbit ZORA approaches can be applied also to the TDDFT methodology, allowing the calculation of singlet−triplet contributions to the UV−vis spectrum.[45−47] This methodology has been already successfully applied by us to evaluate the impact of spin−orbit coupling on the optical properties of the BD and DX1 dyes.[23] In this study we found that although DX1 shows a stronger spin−orbit coupling than BD, the intensity of the low-energy adsorption band is mainly due to a ^{1}MLCT transition, weakly perturbed by spin−orbit coupling.

To provide further insight on the possible role of singlet−triplet transitions in the optical properties of metallorganic Ru(II) and Os(II) dyes, we applied the described computational procedure to a series of realistic polypyridyl dyes. Our attention has been focused first on the analysis of two widely investigated (from both the experimental[14,18,48−68] and theoretical[69−71] points of view) prototype systems for this class of metal−organic complexes: [Ru(bpy)$_3$]$^{2+}$[23,49−51,56−59,63−67,69−73] (**1**) and [Os-(bpy)$_3$]$^{2+}$[18,55,56,60−68,74] (**2**) (see Scheme 1). This investigation has allowed us to evaluate the effects generated by the

B

dx.doi.org/10.1021/jp500869r | J. Phys. Chem. C XXXX, XXX, XXX−XXX

substitution of the metal center within the same coordinating ligands. We then extended our calculations to the "classical" red dye N3[3] (**3**), its Os(II)-based analogous[75,76] (**4**), and an Os(II)-panchromatic dye $[Os(dcbpy)_2(acac)]^{3-}$ (**5**)[77] (see Scheme 1) commonly used to extend light harvesting in the NIR spectral region in the DSC devices. For complex **5**, the effect of the substituents (CF_3 vs CH_3) on the acac ligand has been evaluated, in analogy to what has been done from the experimental side.[77]

This representative selection of Ru(II) and Os(II) complexes allows us to trace a relationship between the molecular structures (different metal centers and/or different ligands and substituents) and the optical properties, quantifying the different spin−orbit coupling for the various complexes and providing a rationale for observable experimental trends. The aim of the present paper is two-fold: (i) to benchmark the methodology for computing the spin−orbit interaction in the optical properties of metal−organic dyes and (ii) to investigate whether the employed methodology can be employed to cast new design rules for next-generation metal−organic solar cell sensitizers.

2. METHODS AND COMPUTATIONAL DETAILS

The Amsterdam Density Functional program package in its latest version (ADF2013) has been used for all calculations.[78−80] The molecular geometries of all the investigated complexes were optimized in the gas phase employing the BP exchange correlation functional (including the Vosko−Wilk−Nusair[81] LDA parametrization and Becke[82] and Perdew[83] gradient corrections to the exchange and correlation, respectively) using the ZORA TZP and DZP basis sets[84] for the metal atoms (the cores 1s−3d for ruthenium and 1s−4d for osmium were kept frozen) and the lighter elements (the 1s core for carbon, nitrogen, and oxygen and 1s−2p for sulfur were kept frozen), respectively.[84] Complexes **1** and **2** were optimized in D_3 symmetry, whereas for complexes **3**, **4**, and **5**, the C_2 symmetry was used. We consider complexes **3**, **4**, and **5** in their tetra-deprotonated form for comparison to the experimental spectra.

In the geometry optimization, the relativistic effects were taken into account by the ZORA Hamiltonian in its scalar approximation.[41,85,86] TDDFT calculations were performed on the BP geometries using the B3LYP (including the Vosko−Wilk−Nusair[81] LDA parametrization and 20% of HF exchange)[87] exchange-correlation functional. We refer the reader to refs 45−47 for additional details of the employed relativistic methodology and its implementation in the ADF code.

Nonrelativistic (NR) TDDFT calculations were also performed on all the investigated complexes (see Supporting Information). Relativistic spectra have been evaluated taking into account the scalar relativistic effects (SR) and including the spin−orbit coupling (SOC) in a self-consistent way. The SOC operator used in the ZORA methodology is expressed as

$$\hat{h}_{SOC} = i\sigma\left(\mathbf{p} \times \frac{c^2}{2c^2 - V}\mathbf{p}\right)$$

(1)

where σ is the Pauli spin matrix vector, $\mathbf{p}$ the moment operator, c the speed of light, and V the Kohn−Sham potential.[47] To obtain a simpler and chemically meaningful description, each SOC transition has been expressed as a linear combination of scalar singlet−singlet and singlet−triplet excitations. Within this

framework, the oscillator strength of the SOC states (f_{SOC}) can be roughly expressed as singlet−triplet transitions borrowing intensity from the coupled singlet−singlet state, and it is approximated by eq 2.

$$f_{SOC} = \frac{\langle\psi_S|\hat{h}_{SOC}|\psi_T\rangle}{E_T - E_S}f_S$$

(2)

f_{SOC} depends directly on the strength of the coupling and inversely on the energy difference between the coupled triplet (T) and singlet states (S). This approach allows us to evaluate accurate excitation energies and oscillator strengths for the SOC states; however, it tends to hide a direct characterization in terms of the corresponding scalar vectors.[88] The strength of the SOC between the spin-free singlet and triplet states is determined by the SOC matrix element, $\langle\psi_{Si}|\hat{h}_{so}|\psi_{Tj}\rangle$. This matrix element has nonzero value if the direct product between the symmetry representations of the three components of ψ_{Si} and ψ_{Tj} transforms as one of the rotation components Rx, Ry, or Rz. For metal complexes in a octahedral coordination, intense SOC states occur only when the coupling singlet and triplet states have the same arriving orbital but a different starting metal d orbital.[37] Moreover, the strength of the matrix element directly depends on the metal content in both singlet and triplet states.

We demonstrated the relevance of including solvation effects in accurately describing the optical properties of Ru(II)-based dyes using a nonrelativistic TDDFT level of calculation.[27] In the present study, solvation effects were included in both TDDFT relativistic and nonrelativistic calculations by the "conductor-like screening model" (COSMO)[89−91] of solvation as implemented in the ADF code.[92] The acetonitrile solvent was considered, thus assigning the ADF default values to the dielectric constant (37.5) and to the radius (2.76 Å) of solvent rigid spheres.

In the simulation of the spectra, we have taken into account the 60−70 lowest singlet−singlet and coupled singlet−triplet transitions, up to an energy over 3.5 eV. The absorption spectra have been simulated by interpolating the computed transitions by Gaussian functions with σ = 0.18 eV roughly corresponding to a full width at half-maximum (FWHM) value of 0.44 eV.

To check the convergence of excitation energies with basis set expansion, TDDFT calculations have been performed (only for complex **1**) by increasing the number of polarization functions both on the metal atom (using the ZORA TZ2P basis set) and on the lighter elements (using the ZORA TZP basis set). The simulated absorption spectra obtained with the extended basis sets are reported in Supporting Information. The results of these tests highlighted only a rigid red-shift of the UV−vis spectrum; we therefore discuss only the TZP-DZP basis set results.

3. RESULTS AND DISCUSSION

3.1. $[Ru(bpy)_3]^{2+}$ and $[Os(bpy)_3]^{2+}$ Benchmarks. The optimized molecular structures of both $[Ru(bpy)_3]^{2+}$ and $[Os(bpy)_3]^{2+}$ are in good agreement with the available X-ray data on these complexes.[48,74] The metal centers experience a quasi-octahedral coordination with Ru−N bond distances of 2.075 Å and Os−N distances of 2.074 Å (compared to mean X-ray values of 2.056 Å[48] and 2.056 Å,[74] respectively). Both the measured and optimized Ru−N distances are almost the same in Ru and Os complexes, and the computed bond lengths deviate from the X-ray values only by less than 0.02 Å. The

computed N−Ru−N bond angles are as follows: 78.3° (the bite angles of each bipyridine), 172.0° (the axial angles), and 90.2° and 96.5° (the angles between the different bpy ligands). These results need to be compared to the X-ray values of 78.6°, 173.0°, 89.1°, and 96.3°, respectively.[48] The optimized N−Os−N bond angles, very similar to those found for the analogous [Ru(bpy)$_3$]$^{2+}$, are 77.8°, 89.7°, and 96.5°, in excellent agreement with the measured data of 77.8(4)°, 90.1(4)°, and 77.8(4)°.[74] The N−Os−N axial angle computed at 172.1° is not reported among the X-ray data.

In Figures 1 and 2 we report the electronic structure of complexes **1** and **2**, respectively, obtained at different levels of
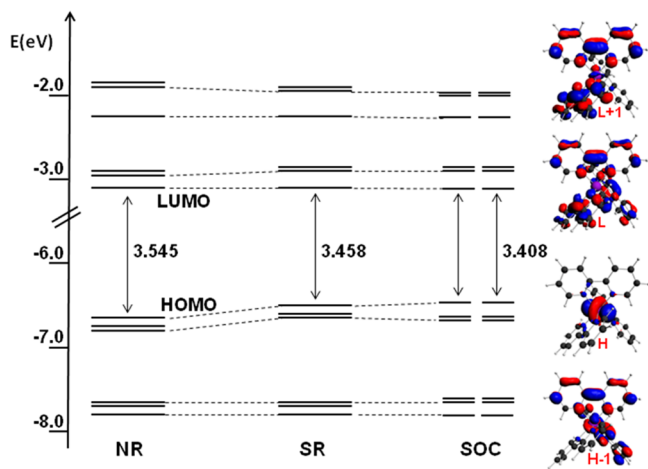

Figure 1. Main frontier molecular orbitals of complex [Ru(bpy)$_3$]$^{2+}$ computed at nonrelativistic (NR) and relativistic levels, both scalar (SR) and including spin−orbit coupling (SOC). Right panel: isodensity plots of selected frontier molecular orbitals computed at the SR level of theory.
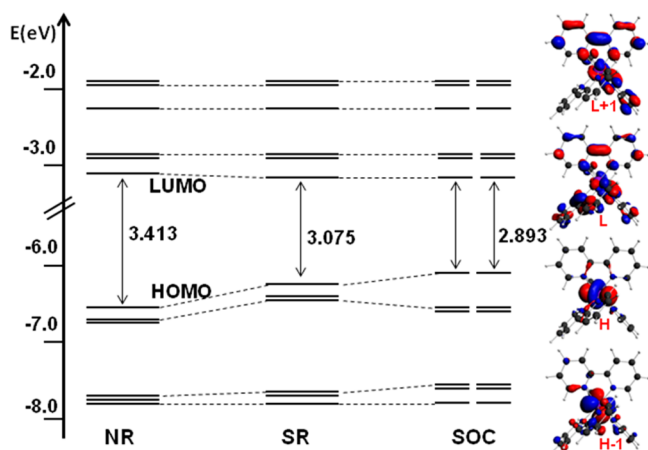

Figure 2. Main frontier molecular orbitals of [Os(bpy)$_3$]$^{2+}$ computed at NR and both relativistic levels, SR and including SOC. Right panel: isodensity plots of selected frontier molecular orbitals computed at the SR level of theory.

calculation. On the left side of each figure, the NR molecular orbitals energies are reported; the center and right portions of the figures contain the relativistic orbitals, SR and SOC, respectively. The energy and character of the main frontier orbitals of both tris-bipyridyl complexes are tabulated in Table 1. It is worth noting that for the Ru complex there are small variations going from the nonrelativistic to the relativistic

orbitals. The main effect can be observed on the SR metal-centered highest occupied molecular orbitals (HOMOs), which are destabilized by about 0.1 eV with respect to the corresponding NR states because of the contraction of the Ru valence shell. As expected, imperceptible energy changes are retrieved in the bpy-based orbitals. Even though the spinors obtained from the SOC calculation cannot be directly related to SR and NR Kohn−Sham orbitals and their characterization is usually not trivial, they can always be associated to the corresponding scalar vectors by projection. From this analysis we found that each spinor is usually well-described by a single scalar molecular orbital, with percentages varying from 70 to 100%.

In contrast to **1**, in the Os(II) complex **2** the SR metal-based orbitals are destabilized by about 0.30 eV with respect to the nonrelativistic counterpart. For this system also the SOC-calculated HOMO results are slightly destabilized (by 0.15 eV) if compared to the corresponding scalar vector. In this case, the spinor is no longer associated to a single scalar orbital, but it is described by a linear combination of the scalar HOMO and HOMO−1/HOMO−2 with different coefficients. Similar considerations can be used to explain the stabilization (0.1 eV) observed for the SOC-calculated HOMO−1 and HOMO−2.

For both complexes, the first HOMOs show consistent contributions from the t$_{2g}$ metal orbitals whereas the lowest unoccupied molecular orbitals (LUMOs) are delocalized on the bpy orbitals (see Figures 1 and 2). The contribution of Ru and Os in the HOMO and HOMO−2 set varies between 72 and 80% and 68−78%, respectively (see Tables 1 and 2).

For both complexes **1** and **2**, the visible bands of the absorption spectra originate from metal-to-ligand charge transfer (MLCT) transitions from the HOMO/HOMO−2 occupied orbitals to the LUMO/LUMO+1 unoccupied ones. In Figure 3, a comparison between the experimental UV−vis spectrum of complex **1** (from ref 49) and the simulated spectra obtained both at the SR- and SOC-TDDFT levels of calculation is reported. Detailed information about the TDDFT transitions are reported in Supporting Information. The experimental spectrum shows a broad band in the 410−470 nm range; the absorption maximum is at 450 nm with a less intense feature at 423 nm. A low-energy tail extends down to 550 nm. The calculated spectra using both SR- and SOC-TDDFT approaches are able to reproduce the experimental visible band, characterized by the superposition of two distinct transitions sets. Observing the intense visible absorption band of complex **1** computed at the SOC-TDDFT level, we can notice that it is slightly blue-shifted with respect to the SR one and its intensity slightly decreased. In the low-energy region, the weak band tail slightly increases its intensity, better matching the experimental spectrum. It is worth noting that the SOC-perturbed states borrow their intensity from those of the SR singlet−singlet allowed states; therefore, the average intensity of the simulated spectra obtained at both approaches is the same even though it shows a different distribution. The NR simulated spectrum (Supporting Information) is further blue-shifted with respect to the relativistic ones and does not show the low-energy tail.

Inspection of the SR-TDDFT eigenvectors (Supporting Information) reveals that the visible absorption band is originated by two pairs of degenerate transitions, two at 447 nm with f = 0.11 and two at 425 nm with f = 0.18. These two pairs of singlet−singlet (S) excited states, essentially described

Table 1. Energy and Character of the Main Frontier Molecular Orbitals of $[Ru(bpy)_3]^{2+}$ and $[Os(bpy)_3]^{2+}$ Computed at the NR and SR Levels of Theory in D_3 Symmetry

	$[Ru(bpy)_3]^{2+}$ NR					
	HOMO−2 (31e)	HOMO−1 (31e)	HOMO (17a$_1$)	LUMO (16a$_2$)	LUMO+1 (32e)	LUMO+2 (32e)
E (eV)	−6.766	−6.766	−6.640	−3.095	−2.943	−2.943
% Ru	44d$_{x^2-y^2}$	44d$_{xy}$	80d$_{z^2}$		3d$_{x^2-y^2}$	3d$_{xy}$
	28 d$_{yz}$	28d$_{xz}$			2d$_{yz}$	2d$_{xz}$
% bpy	16	16	11	94	85	85
	$[Ru(bpy)_3]^{2+}$ SR					
	HOMO−2 (31e)	HOMO−1 (31e)	HOMO (17a$_1$)	LUMO (16a$_2$)	LUMO+1 (32e)	LUMO+2 (32e)
E (eV)	−6.665	−6.665	−6.546	−3.088	−2.920	−2.920
% Ru	44d$_{x^2-y^2}$	44d$_{xy}$	80d$_{z^2}$		4d$_{x^2-y^2}$	4d$_{xy}$
	28d$_{yz}$	28d$_{xz}$			3d$_{yz}$	3d$_{xz}$
% bpy	17	17	12	88	89	89
	$[Os(bpy)_3]^{2+}$ NR					
	HOMO−2 (33e)	HOMO−1 (33e)	HOMO (18a$_1$)	LUMO (18a$_2$)	LUMO+1 (34e)	LUMO+2 (34e)
E (eV)	−6.715	−6.715	−6.550	−3.137	−2.923	−2.923
% Os	42d$_{x^2-y^2}$	42d$_{xy}$	77d$_{z^2}$	1p$_z$	4d$_{x^2-y^2}$	4d$_{xy}$
	27d$_{yz}$	27d$_{xz}$			3d$_{yz}$	3d$_{xz}$
% bpy	20	20	13	81	85	85
	$[Os(bpy)_3]^{2+}$ SR					
	HOMO−2 (33e)	HOMO−1 (33e)	HOMO (18a$_1$)	LUMO (18a$_2$)	LUMO+1 (34e)	LUMO+2 (34e)
E (eV)	−6.437	−6.437	−6.253	−3.178	−2.907	−2.907
% Os	41d$_{x^2-y^2}$	41d$_{xy}$	78d$_{z^2}$		5d$_{x^2-y^2}$	5d$_{xy}$
	27d$_{yz}$	27d$_{xz}$			4d$_{yz}$	4d$_{xz}$
% bpy	20	20	13	88	91	91

by HOMO−1 → LUMO and HOMO−1 → LUMO+1 transitions, respectively, show, as expected, a prevalent MLCT character. Upon inclusion of SOC, we find that the excitation at 425 nm is only slightly blue-shifted and reduced in intensity with respect to the scalar one, but it essentially preserves its singlet−singlet character. On the contrary, we found that a stronger coupling is present for the excited state at 447 nm: we computed three doubly degenerate SOC-transitions at 455, 446, and 442 nm whose intensities sum equals the intensity of the SR transition. Two SOC degenerate transitions are calculated at 502 nm (f = 0.003) and 498 nm (f = 0.006), which together with two transitions found at 489 nm (f = 0.003) and 463 nm (f = 0.002) constitutes the low-energy tail. The lowest-energy excitations (502 and 498 nm) have essential SR-triplet character resulting from the mixing of a series of low-energy triplet states with small percentages of intense higher-lying SR-singlet MLCT states (0.15−0.40 eV above the lowest SR-triplet state). The transitions at 489 and 463 nm show relevant contributions from SR-singlet states which are closer in energy but characterized by low oscillator strengths. Thus, the SOC states of both groups of transitions have a reduced intensity but for different reasons. A larger coupling is instead observed in the 400−460 nm region of the spectrum, which is dominated by SOC. Additional features in the low-energy region of the $[Ru(bpy)_3]^{2+}$ spectrum could be attributed to vibronic effects which are not included in our simulation toolbox.[71]

In Figure 4 we report the computed SR and SOC spectra of the $[Os(bpy)_3]^{2+}$ complex **2** along with experimental data.[68] The experimental spectrum shows two close bands at ca. 450 and 490 nm and a less intense band between 550 and 700 nm.[68] The SR calculations reproduce the intense visible band at 454−494 nm but clearly miss the low-energy band. This band is instead nicely reproduced upon inclusion of SOC, Figure 4,

which also introduces an intensity redistribution in the higher-energy range. The experimental band spanning the region 550−700 nm is fairly well reproduced by SOC-TDDFT calculations. This band is mainly originated by transitions at 622 nm (f = 0.015), 590 nm (f = 0.021), 488 nm (f = 0.060), and 482 nm (f = 0.058), one order of magnitude more intense than those corresponding to the Ru(II) analogue. For complex **2**, the interacting singlet states are characterized by larger oscillator strengths, larger mixing percentages, and reduced $E_T - E_S$. In addition to the heavy-atom effect, this contributes to generate a larger SOC effect on the absorption spectrum.

3.2. Optical Properties of the N3 Dye and of Its Osmium Analogue. We now turn to investigate two prototypical dyes effectively employed in DSCs, i.e., the ruthenium N3 dye and its osmium analogue. Here we focus on the spectral changes associated with the different metals and the different ligands experienced by the metal center with respect to the tris-bipyridine complexes.
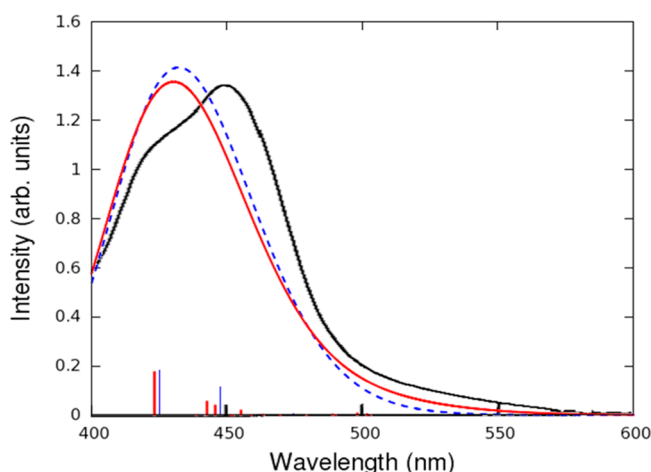
N3 dye has been widely investigated by theoretical studies, and the electronic and optical properties of this complex, also in its fully deprotonated form, have been analyzed at different levels of theory.[27,29,30,93] Nevertheless, to our knowledge, no calculations including SOC have been reported.

The electronic structure of the fully deprotonated form of N3, $[Ru(dcbpy)_2(SCN)_2]^{4-}$, **3**, is reported in Figure 5.

The occupied orbitals of complex **3** can be classified into two sets of three mixed metal-SCN π orbitals, resulting from the bonding (HOMO−4/HOMO−6) and antibonding combinations (HOMO/HOMO−2) of Ru-t$_{2g}$ orbitals with the p orbitals of the SCN ligands. The HOMO−4/HOMO−6, moreover, show a sizable density contribution from the COO$^-$ terminal groups. An exclusive SCN π orbital (representing the HOMO−3 complex orbital) inserts between the two metal−ligand orbital sets. The LUMOs are almost entirely delocalized

Table 2. Energy and Character of the Main Frontier Molecular Orbitals of $[Ru(dcbpy)_2(SCN)_2]^{4-}$ and $[Os(dcbpy)_2(SCN)_2]^{4-}$ Computed at the Nonrelativistic and Scalar Levels of Theory within C_2 Symmetry

	$[Ru(dcbpy)_2(SCN)_2]^{4-}$ NR					
	HOMO-2 (56a)	HOMO-1 (56b)	HOMO (57a)	LUMO (57b)	LUMO+1 (58a)	LUMO+2 (58b)
E (ev)	−5.696	−5.624	−5.432	−2.551	−2.454	−1.696
% Ru	$33d_{xy}$	$44d_{yz}$	$31d_{z^2}$	$3d_{yz}$	$3d_{z^2}$	
	$6d_{x^2-y^2}$		$8d_{xy}$		$2d_{x^2-y^2}$	
	$2d_{z^2}$		$7d_{x^2-y^2}$		$1d_{xy}$	
% bpy	2	4	7	82	74	87
% SCN	49	43	41			

	$[Ru(dcbpy)_2(SCN)_2]^{4-}$ SR					
	HOMO-2 (56a)	HOMO-1 (56b)	HOMO (57a)	LUMO (57b)	LUMO+1 (58a)	LUMO+2 (58b)
E (eV)	−5.615	−5.538	−5.341	−2.524	−2.417	−1.677
% Ru	$35d_{xy}$	$47d_{yz}$	$32d_{z^2}$	$3d_{yz}$	$3d_{z^2}$	
	$6d_{x^2-y^2}$		$9d_{xy}$		$2d_{x^2-y^2}$	
	$2d_{z^2}$		$6d_{x^2-y^2}$		$2d_{xy}$	
% dcbpy	5	6	10	85	80	88
% SCN	44	39	36			

	$[Os(dcbpy)_2(SCN)_2]^{4-}$ NR					
	HOMO-2 (59a)	HOMO-1 (60b)	HOMO (60a)	LUMO (61b)	LUMO+1 (61a)	LUMO+2 (62b)
E (eV)	−5.620	−5.545	−5.315	−2.556	−2.456	−1.694
% Ru	$33d_{xy}$	$44d_{yz}$	$30d_{z^2}$	$4d_{yz}$	$4d_{z^2}$	
	$5d_{x^2-y^2}$		$9d_{xy}$		$2d_{x^2-y^2}$	
	$2d_{z^2}$		$6d_{x^2-y^2}$		$2d_{xy}$	
% dcbpy	5	6	10	81	78	91
% SCN	47	42	41			

	$[Os(dcbpy)_2(SCN)_2]^{4-}$ SR					
	HOMO-2 (59a)	HOMO-1 (60b)	HOMO (60a)	LUMO (61b)	LUMO+1 (61a)	LUMO+2 (62b)
E (eV)	−5.423	−5.341	−5.106	−2.548	−2.423	−1.693
% Ru	$37d_{xy}$	$50d_{yz}$	$31d_{z^2}$	$6d_{yz}$	$5d_{z^2}$	
	$7d_{x^2-y^2}$		$13d_{xy}$		$3d_{x^2-y^2}$	
	$3d_{z^2}$		$5d_{x^2-y^2}$		$2d_{xy}$	
% dcbpy	7	9	11	84	77	91
% SCN	33	32	34			

Figure 3. Comparison between the experimental (black line) and the computed UV−vis spectra of the $[Ru(bpy)_3]^{2+}$ complex. SR (blue dashed line) and SOC (red line) spectra are reported. The experimental spectrum from ref 49 has been scaled to match the intensity of the lowest absorption band of the SOC-calculated spectrum.
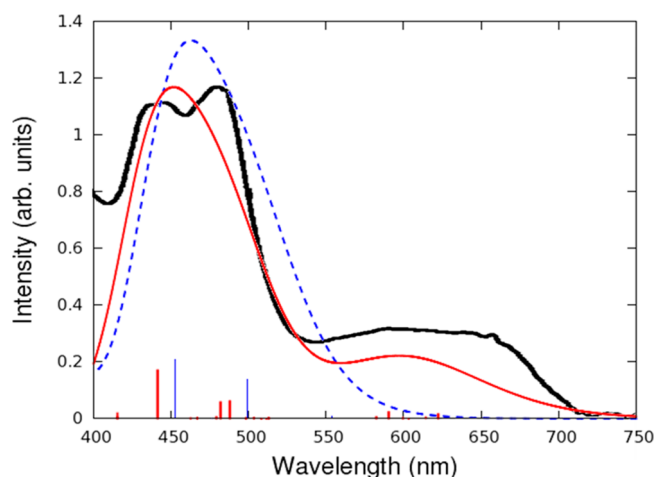
Figure 4. Comparison between the experimental (black line) and the computed UV−vis spectra of the $[Os(bpy)_3]^{2+}$ complex. SR spectrum is the blue dashed line; the spectrum including spin−orbit coupling is the red line. The experimental spectrum, taken from ref 68, has been scaled to match the intensity of the SOC-calculated visible absorption band.

on the dcbpy ligands, apart from small Ru percentages present in the LUMO and LUMO+1 (Figure 5 and Table 2).

The inclusion of relativistic effects slightly destabilizes the two sets of mixed Ru-SCN HOMOs. The same effect can be observed also for the LUMO and LUMO+1 orbitals. Having in
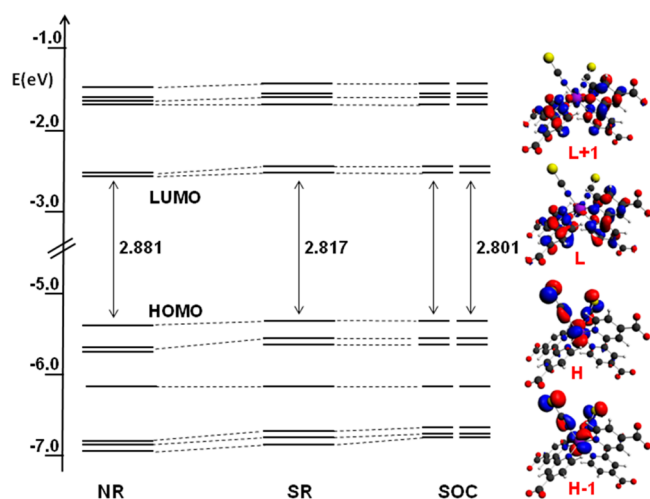
Figure 5. Main frontier molecular orbitals of $[Ru(dcbpy)_2(SCN)_2]^{4-}$ computed at NR, SR, and SO levels of calculation. Right panel: isodensity plots of selected frontier molecular orbitals computed at the SR level of theory.

mind the nature of the first HOMOs and LUMOs, we can then conclude that the orbitals containing metal character are those mainly affected by the inclusion of relativity.

Also for the analogous complex, **4**, we analyzed the electronic structure at the nonrelativistic level and at both SR and SOC level of calculations; the computed frontier molecular orbitals are reported in Figure 6. We notice that a slight energy
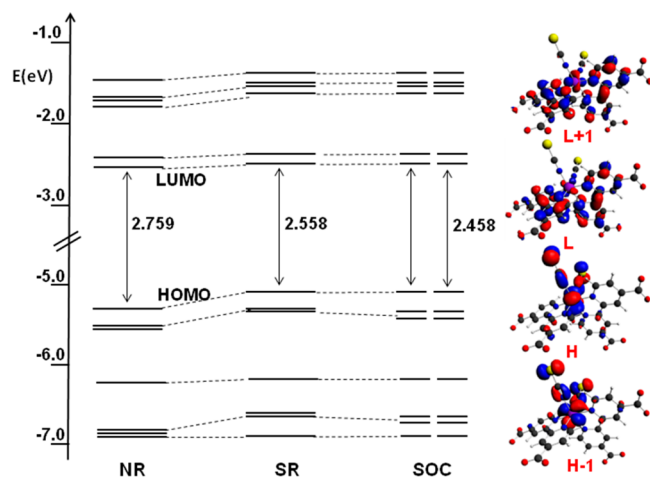

Figure 6. Main frontier molecular orbitals of $[Os(dcbpy)_2(SCN)_2]^{4-}$ computed at NR, SR, and SOC levels of calculation. Right panels: isodensity plots of selected frontier molecular orbitals computed at the SR level of theory.

destabilization (0.03−0.08 eV) is computed for the HOMO−1/HOMO−2 and HOMO−4/HOMO−5 orbitals upon inclusion of SOC, although the largest differences are found going from NR to SR calculations.

In Figure 7, the comparison between the experimental absorption spectrum of **3** in ethanol[94] and the spectra simulated at the SR and SOC levels is reported. Both calculated spectra fairly reproduce the main features of the experimental spectrum, which is characterized by an intense band at about 510 nm. Small differences can be observed only in the lower-energy range (570−700 nm) where the calculated tail, both at
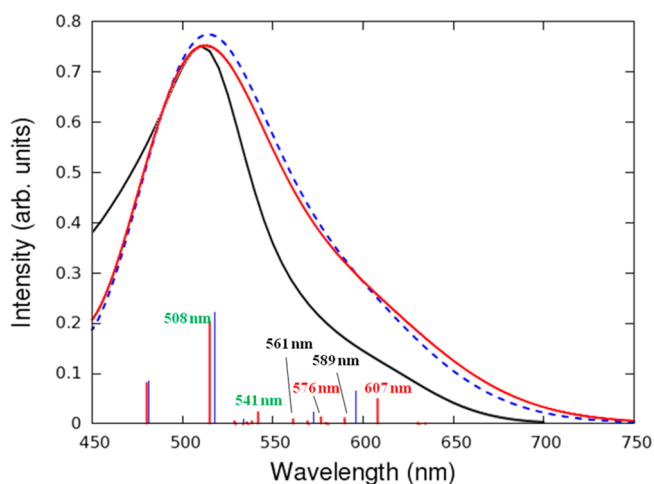

Figure 7. Comparison between the experimental (black line) spectrum taken from ref 94 and the computed relativistic spectra of $[Ru(dcbpy)_2(SCN)_2]^{4-}$. The scalar spectrum is the blue dashed line; the spectrum including spin−orbit coupling is the red line. The experimental spectrum has been scaled to match the intensity of the SOC-calculated one.

SR and SOC levels of theory, is slightly red-shifted with respect to the experiment. Also, the intensities of the tail are slightly overestimated.

In this case, SOC inclusion does not dramatically affect the calculated spectrum, producing only small intensity decreases and a red-shift of the scalar features, in particular in the lower-energy region. From the analysis of the SOC eigenvectors we have been able to fully characterize the various transitions giving rise to the simulated spectra. In the low-energy region (λ > 610 nm), we computed a series of SOC transitions characterized by low oscillator strengths due to the small contributions from the SR singlet−singlet excitations. More intense SOC transitions are found at higher energies. As an example, the SOC excitations at 607 and 576 nm originate from the mixing (with different percentages) of the SR S_1 and T_3 states. The S_1 excited state has the HOMO as the starting state, whereas T_3 has the HOMO−1, but both have the LUMO as the arriving orbital. It is important to point out that the results obtained in this work for the Ru(II) complexes are in perfect agreement with those calculated by us in ref 23 for the BD and DX1 sensitizers. Indeed, also in these cases we found that the inclusion of SOC produces only fine changes of the absorption bands that are useful for accurately reproducing the features of the experimental spectrum but are not able to qualitatively change its structure.

When the Ru center is substituted by Os the experimental spectrum shows a new band at lower energy which extends up to about 1000 nm (Figure 8.)[75] Also in this case the SR-calculated spectrum, showing only an intense low-energy feature at about 700 nm, is not able to explain the experimental absorption band which includes the 650−1000 nm region. Equivalent to the $[Os(bpy)_3]^{2+}$ complexes, only the inclusion of SOC allows us to quantitatively reproduce the experimental low-energy absorption band of complex **4** (Figure 8). For this system, SOC is relevant also to properly describe the features of the MLCT intense band in the visible region of the spectrum, which is consistently blue-shifted with respect to that provided by SR-TDDFT calculations. We can thus conclude that for Os(II) complexes inclusion of SOC effects is mandatory, even
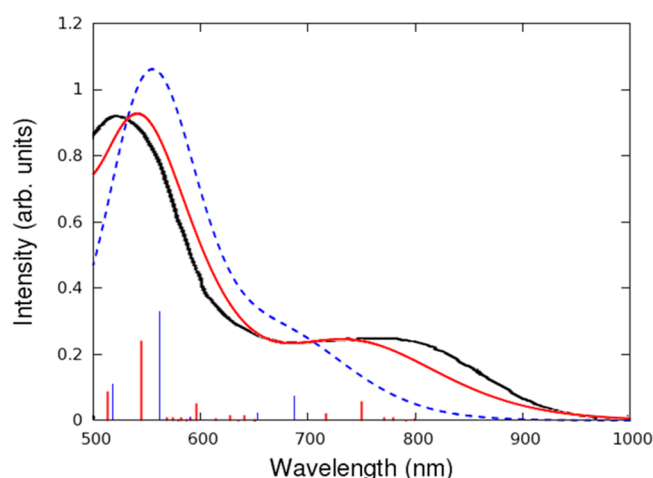
Figure 8. Comparison between the experimental spectrium (black line) taken from ref 75 and the computed relativistic spectra of the $[Os(dcbpy)_2(SCN)_2]^{4-}$. Scalar spectrum is the blue dashed line, and the spectrum including spin−orbit coupling is the red line. The experimental spectrum has been scaled to match the intensity of the SOC-calculated visible absorption band.

Figure 9. Main frontier molecular orbitals of $[Os(dcbpy)_2(acac)]^{3-}$ computed at SR and SOC levels of calculation. Left panel: isodensity plots of selected frontier molecular orbitals computed at the SR level of theory.

to get a qualitative description of the UV−vis absorption spectrum.

The obtained results suggest that the effect of SOC on the spectrum is mainly related to the metal atom involved in the complex. This behavior can be easily explained considering that the heavier the metal is, the faster its electrons are and the stronger the magnetic field generated by them is; consequently, the corresponding SOC matrix elements ($\langle\psi_{Si}|\hat{h}_{so}|\psi_{Tj}\rangle$) are larger. However, despite being small, the observed changes in the SOC effects can be observed also for complexes containing the same metal center but different ligands. These subtle differences could be due to changes in the relative positions of the scalar singlet and triplet states resulting in different $E_S - E_T$ denominators in eq 2, and these second-order effects are probably related to different coordinating ligands with different charge donation/back-donation flows, as is the case of the previously reported DX1 dye.[23]

3.3. $[Os(dcbpy)_2(acac)]^{3-}$ Panchromatic Dye. In this section we focus our attention on an interesting Os(II) sensitizer belonging to the Os panchromatic dyes class: $[Os(dcbpy)_2(acac)]^{3-}$, **5**.[77] Because the experimental data refer to pH 12, we have taken into account the fully deprotonated species. As for the previous systems, we started our study of the electronic structure of the sensitizer **5** from the analysis of the main frontier orbitals obtained both at SR and SOC levels of theory (Figure 9). The SR HOMO−HOMO−2 are Os-based orbitals whose metal contributions vary from 59% (HOMO−1) to 74% (HOMO−2); completely different behavior is observed for the HOMO−3 orbital showing only 8% Os character (left side of Figure 9). Sizable percentages of π orbitals of both acac and dcbpy ligands are present in the HOMO−HOMO−2 orbitals. The scalar LUMO/LUMO+1 are almost degenerate and are mainly delocalized on the dcbpy ligands (ca. 80%) with sizable percentages of Os t_{2g} orbitals. The LUMOs at higher energies reported in Figure 9 are delocalized on the acac ligands with decreasing metal content from 3% to 1%.

The spinors in the right side of Figure 9 are very similar in character to the related scalar orbitals, and as observed for the
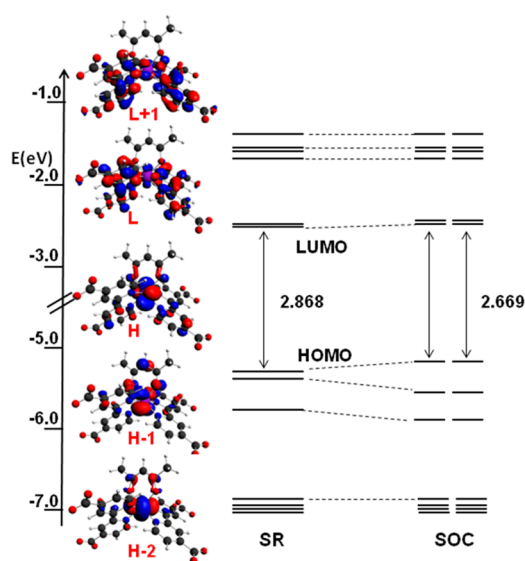
other investigated Os complexes, their energy shifts directly depending on the amount of metal character.

In Figure 10 the comparison between the experimental[77] and both the SR and SOC-computed spectra is reported. As
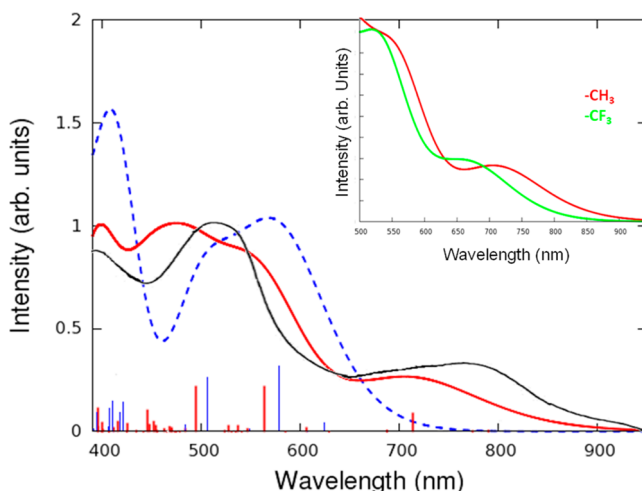

Figure 10. Comparison between the experimental spectrum (black line) taken from ref 77 and the computed relativistic spectra of $[Os(dcbpy)_2(acac)]^{3-}$ (SR spectrum in blue dashed line and spectrum including SOC in red line). The experimental spectrum has been scaled to match the intensity of the SOC-calculated visible absorption band.

observed for other investigated Os-based complex, inclusion of SOC is fundamental for describing all the features present in the experimental spectrum of complex **5**, in particular to reproduce the low-energy absorption band completely neglected by a SR approach. This is evident considering that the lowest SR singlet−singlet excitation can be found at 623 nm, whereas the experimental spectrum maintains a sizable intensity also in energy regions beyond 900 nm. On the other hand, the lowest SOC transition lies at 803 nm even though it shows an almost negligible oscillator strength. Furthermore, in

the SOC-TDDFT calculations, we computed two excitations at 789 and 773 nm (characterized by low intensities of 0.004 and 0.002, respectively), clearly related to the lowest-energy part of the experimental absorption band ranging from 660 to 900 nm. A more intense excitation at 712 nm is also present. The character of the main SOC excitations in terms of the involved SR excited states and molecular orbitals are reported in Supporting Information. The SOC transitions at 789 and 773 nm result from the coupling between the lowest-energy S_1 and T_1/T_2 excitations, respectively. The transition at 712 nm combines instead the SR T_3 excitation at 666 nm (63%) with the SR S_3 and S_1 states at 578 nm (11%) and 624 nm (7%), respectively. These scalar states have MLCT character, involving HOMO/HOMO−1 as starting states and LUMO/LUMO+1 as arriving states. The two SOC main transitions characterized by comparable intensities ($f = 0.216$ and 0.220, respectively) are computed at 563 and 494 nm. The former excitation can be described as the mixing between the S_3 excited state (HOMO; HOMO−1 → LUMO+1; LUMO) at 578 nm (47%) and T_3/T_5 states at 666 nm (25%) and 559 nm (14%), respectively, involving HOMO, HOMO−1, and HOMO−2 as starting orbitals. The SOC excitation at 494 nm shows instead a reduced mixing of the SR states being for the 84% described by the intense singlet−singlet state S_5 at 506 nm. The intensity of this SR transition is conserved in the related SOC transition. All these excited states involve essentially the metal-based HOMOs as starting states and the pair LUMO/LUMO+1 as arriving states and therefore can be characterized as MLCT transitions from Os orbitals to the dcbpy ligands.

To evaluate the effect of different functional groups on the acac ligand in relation to dyes of experimental interest, we investigated also the $[Os(dcbpy)2(tfac)]^{3-}$ dye, characterized by the substitution of the methyl moiety with the −CF$_3$ one in the acac moiety. It has been experimentally observed that the substitution of −CH$_3$ by −CF$_3$ shifts the Os$^{3+/2+}$ oxidation potential to more positive values, making the dye regeneration process more efficient.[77] The experimental spectrum of $[Os(dcbpy)2(tfac)]^{3-}$ shows a low-energy absorption band in the range of 620−900 nm blue-shifted with respect to that of complex **5**. The simulated spectrum of $[Os(dcbpy)2(tfac)]^{3-}$ is reported in the inset of Figure 10 compared to that of complex **5**; also in this case the TDDFT-SOC methodology has been able to reproduce the slight blue-shift observed in the experimental spectrum.[77]

4. CONCLUSIONS

We have examined the effect of relativistic effects on the TDDFT-simulated absorption spectrum of a series of Ru(II) and Os(II) polypyridyl complexes employed as solar cell sensitizers in dye-sensitized solar cells. We started our analysis from the widely investigated $[M(bpy)_3]^{2+}$ (M = Ru and Os) complexes, on which we benchmarked our computational approach. We then moved to the examination of realistic dyes (N3, the Os-based analogue, and $[Os(dcbpy)_2(acac)]^{3-}$) effectively used in DSCs.

The simulation of the optical absorption spectra has been performed by TDDFT calculations using the 2-component ZORA relativistic Hamiltonian, taking into account solvation effects by means of a dielectric continuum model. The employed strategy permits also the evaluation, in a separate way, of the changes in the absorption bands associated with scalar relativistic effects from those related to the spin−orbit

coupling. This theoretical approach allowed us to accurately reproduce and interpret the main features of the experimental absorption spectra, assigning the spin−orbit coupled transitions by projection on the corresponding scalar vectors.

We found that the inclusion of relativistic effects, and in particular of spin−orbit coupling, is fundamental even for a qualitatively correct reproduction of the experimental absorption spectrum of Os(II) complexes. Spin−orbit coupling effects are found to be substantially less important in determining the optical properties of complexes containing the lighter Ru(II) center. For these systems, spin−orbit coupling does not strongly change the general structure of the spectrum, but rather it contributes some system-dependent modulation of the low-energy spectral region. The small but sizable system-dependent variations are assigned to ligand-based electronic structure modifications resulting in a different relative position of the (scalar relativistic) singlet and triplet states with consequent effects on their coupling.

We believe the employed computational strategy is a powerful tool for evaluating the effects of relativity and in particular of spin−orbit coupling on the absorption spectrum of metal complexes containing heavy elements. Moreover, we believe that this approach could be extremely useful for designing new and efficient sensitizers characterized by enhanced absorption in the red part of the solar spectrum.

■ ASSOCIATED CONTENT

⑤ Supporting Information

Tables reporting the main scalar and spin orbit transitions for all the investigated complexes, nonrelativistic computed spectra for complexes **1−4**, and scalar relativistic spectra of $[Ru(bpy)_3]^{2+}$ computed with different basis sets. This material is available free of charge via the Internet at http://pubs.acs.org.

■ AUTHOR INFORMATION

Corresponding Author

*E-mail: simona@thch.unipg.it.

Notes

The authors declare no competing financial interest.

■ ACKNOWLEDGMENTS

■ REFERENCES

(1) O'Regan, B.; Grätzel, M. A Low-Cost, High-Efficiency Solar Cell Based on Dye-Sensitized Colloidal TiO$_2$ Films. *Nature* **1991**, *353*, 737−740.

(2) Grätzel, M. Photoelectrochemical Cells. *Nature* **2001**, *414*, 338−344.

(3) Nazeeruddin, M. K.; De Angelis, F.; Fantacci, S.; Selloni, A.; Viscardi, G.; Liska, P.; Ito, S.; Takeru, B.; Grätzel, M. Combined Experimental and DFT-TDDFT Computational Study of Photoelectrochemical Cell Ruthenium Sensitizers. *J. Am. Chem. Soc.* **2005**, *127*, 16835−16847.

(4) Yella, A.; Lee, H.-W.; Tsao, H. N.; Yi, C.; Chandiran, A. K.; Nazeeruddin, M. K.; Diau, E. W.-G.; Yeh, C.-Y.; Zakeeruddin, S. M.; Grätzel, M. Porphyrin-Sensitized Solar Cells with Cobalt$^{(II/III)}$ Based Redox Electrolyte Exceed 12% Efficiency. *Science* **2011**, *334*, 629−634.

(5) Kinoshita, T.; Fujisawa, J.-I.; Nakazaki, J.; Uchida, S.; Kubo, T.; Segawa, H. Enhancement of Near-IR Photoelectric Conversion in Dye-Sensitized Solar Cells Using an Osmium Sensitizer with Strong Spin-Forbidden Transition. *J. Phys. Chem. Lett.* **2012**, *3*, 394−398.

(6) Nazeeruddin, M. K.; Péchy, P.; Renouard, T.; Zakeeruddin, S. M.; Humphry-Baker, R.; Comte, P.; Liska, P.; Cevey, L.; Costa, E.; Shklover, V.; et al. Engineering of Efficient Panchromatic Sensitizers for Nanocrystalline TiO2-Based Solar Cells. *J. Am. Chem. Soc.* 2001, 123, 1613−1624.

(7) Abbotto, A.; Sauvage, F.; Barolo, C.; De Angelis, F.; Fantacci, S.; Graetzel, M.; Manfredi, N.; Marinzi, C.; Nazeeruddin, M. K. Panchromatic Ruthenium Sensitizer Based on Electron-Rich Heteroarylvinylene π-Conjugated Quaterpyridine for Dye-Sensitized Solar Cells. *Dalton Trans.* 2011, 40, 234−242.

(8) Altobello, S.; Argazzi, R.; Caramori, S.; Contado, C.; Da Fré, S.; Rubino, P.; Choné, C.; Larramona, G.; Bignozzi, C. A. Sensitization of Nanocrystalline TiO2 with Black Absorbers Based on Os and Ru Polypyridine Complexes. *J. Am. Chem. Soc.* 2005, 127, 15342−15343.

(9) Chen, B.-S.; Chen, K.; Hong, Y.-H.; Liu, W.-H.; Li, T.-H.; Lai, C.-H.; Chou, P.-T.; Chi, Y.; Lee, G.-H. Neutral, Panchromatic Ru(II) Terpyridine Sensitizers Bearing Pyridine Pyrazolate Chelates with Superior DSSC Performance. *Chem. Commun.* 2009, 5844.

(10) Chou, C.-C.; Wu, K.-L.; Chi, Y.; Hu, W.-P.; Yu, S. J.; Lee, G.-H.; Lin, C.-L.; Chou, P.-T. Ruthenium(II) Sensitizers with Heteroleptic Tridentate Chelates for Dye-Sensitized Solar Cells. *Angew. Chem., Int. Ed.* 2011, 50, 2054.

(11) Kinoshita, T.; Dy, J. T.; Uchida, S.; Kubo, T.; Segawa, H. Wideband Dye-Sensitized Solar Cells Employing a Phosphine-Coordinated Ruthenium Sensitizer. *Nat. Photonics* 2013, 7, 535−539.

(12) Funaki, T.; Yanagida, M.; Onozawa-Komatsuzaki, N.; Kasuga, K.; Kawanishi, Y.; Kurashige, M.; Sayama, K.; Sugihara, H. Synthesis of a New Class of Cyclometallated Ruthenium(II) Complexes and Their Application in Dye-Sensitized Solar Cells. *Inorg. Chem. Commun.* 2009, 12, 842−845.

(13) Funaki, T.; Funakoshi, H.; Kitao, O.; Onozawa-Komatsuzaki, N.; Kasuga, K.; Sayama, K.; Sugihara, H. Cyclometalated Ruthenium-(II) Complexes as Near-IR Sensitizers for High Efficiency Dye-Sensitized Solar Cells. *Angew. Chem., Int. Ed.* 2012, 51, 7528−7531.

(14) Johansson, E. M. J.; Odelius, M.; Plogmaker, S.; Gorgoi, M.; Svensson, S.; Siegbahn, H.; Rensmo, H. Spin−Orbit Coupling and Metal−Ligand Interactions in Fe(II), Ru(II), and Os(II) Complexes. *J. Phys. Chem. C* 2010, 114, 10314−10322.

(15) Onicha, A. C.; Castellano, F. N. Electrolyte-Dependent Photovoltaic Responses in Dye-Sensitized Solar Cells Based on an Osmium(II) Dye of Mixed Denticity. *J. Phys. Chem. C* 2010, 114, 6831−6840.

(16) Nazeeruddin, M. K.; Pechy, P.; Grätzel, M. Efficient Panchromatic Sensitization of Nanocrystalline TiO2 Films by a Black Dye Based on a Trithiocyanato−Ruthenium Complex. *Chem. Commun.* 1997, 1705−1706.

(17) Zubavichus, Y. V.; Slovokhotov, Y. L.; Nazeeruddin, M. K.; Zakeeruddin, S. M.; Grätzel, M.; Shklover, V. Structural Characterization of Solar Cell Prototypes Based on Nanocrystalline TiO2 Anatase Sensitized with Ru Complexes. X-ray Diffraction, XPS, and XAFS Spectroscopy Study. *Chem. Mater.* 2002, 14, 3556−3563.

(18) Bauer, C.; Boschloo, G.; Mukhtar, E.; Hagfeldt, A.; Bauer, C.; Boschloo, G.; Mukhtar, E.; Hagfeldt, A. Interfacial Electron-Transfer Dynamics in Ru(tcterpy)(NCS)(3)-Sensitized TiO2 Nanocrystalline Solar Cells. *J. Phys. Chem. B* 2002, 106, 12693−12704.

(19) Han, L.; Islam, A.; Chen, H.; Malapaka, C.; Chiranjeevi, B.; Zhang, S.; Yang, X.; Yanagida, M. High-Efficiency Dye-Sensitized Solar Cell with a Novel Co-Adsorbent. *Energy Environ. Sci.* 2012, 5, 6057−6060.

(20) Barolo, C.; Nazeeruddin, M. K.; Fantacci, S.; Di Censo, D.; Comte, P.; Liska, P.; Viscardi, G.; Quagliotto, P.; De Angelis, F.; Ito, S.; et al. Synthesis, Characterization, and DFT-TDDFT Computational Study of a Ruthenium Complex Containing a Functionalized Tetradentate Ligand. *Inorg. Chem.* 2006, 45, 4642−4653.

(21) Abbotto, A.; Barolo, C.; Bellotto, L.; De Angelis, F.; Gratzel, M.; Manfredi, N.; Marinzi, C.; Fantacci, S.; Yum, J. H.; Nazeeruddin, M. K. Electron-Rich Heteroaromatic Conjugated Bipyridine Based Ruthenium Sensitizer for Efficient Dye-Sensitized Solar Cells. *Chem. Commun.* 2008, 5318−5320.

(22) Fantacci, S.; Lobello, M. G.; De Angelis, F. Everything You Always Wanted to Know About Black Dye (but Were Afraid to Ask): A DFT/TDDFT Investigation. *Chimia* 2013, 67, 121−128.

(23) Fantacci, S.; Ronca, E.; De Angelis, F. Impact of Spin−Orbit Coupling on Photocurrent Generation in Ruthenium Dye-Sensitized Solar Cells. *J. Phys. Chem. Lett.* 2014, No. 5, 375−380.

(24) Li, M.-X.; Zhou, X.; Xia, B.-H.; Zhang, H.-X.; Pan, Q.-J.; Liu, T.; Fu, H.-G.; Sun, C.-C. Theoretical Studies on Structures and Spectroscopic Properties of Photoelectrochemical Cell Ruthenium Sensitizers, [Ru(H$_m$tcterpy)(NCS)$_3$]$^{n-}$ (m = 0, 1, 2, and 3; n = 4, 3, 2, and 1). *Inorg. Chem.* 2008, 47, 2312−2324.

(25) Presselt, M.; Dietzek, B.; Schmitt, M.; Rau, S.; Winter, A.; Jäger, M.; Schubert, U. S.; Popp, J. A Concept to Tailor Electron Delocalization: Applying QTAIM Analysis to Phenyl−Terpyridine Compounds. *J. Phys. Chem. A* 2010, 114, 13163−13174.

(26) Escudero, D.; González, L. RASPT2/RASSCF vs Range-Separated/Hybrid DFT Methods: Assessing the Excited States of a Ru(II)bipyridyl Complex. *J. Chem. Theory Comput.* 2012, 8, 203−213.

(27) Fantacci, S.; De Angelis, F.; Selloni, A. Absorption Spectrum and Solvatochromism of the [Ru(4,4'-COOH-2,2'-bpy)$_2$(NCS)$_2$] Molecular Dye by Time Dependent Density Functional Theory. *J. Am. Chem. Soc.* 2003, 125, 4381−4387.

(28) Fantacci, S.; De Angelis, F. A Computational Approach to the Electronic and Optical Properties of Ru(II) and Ir(III) Polypyridyl Complexes: Applications to DSC, OLED and NLO. *Coord. Chem. Rev.* 2011, 255, 2704−2726.

(29) De Angelis, F.; Fantacci, S.; Selloni, A.; Nazeeruddin, M. K. Time Dependent Density Functional Theory Study of the Absorption Spectrum of the [Ru(4,4'-COO⁻-2,2'-bpy)$_2$ (X)$_2$]$^{4−}$ (X = NCS, Cl) Dyes in Water Solution. *Chem. Phys. Lett.* 2005, 415, 115−120.

(30) De Angelis, F.; Fantacci, S.; Selloni, A. Time-Dependent Density Functional Theory Study of the Absorption Spectrum of [Ru(4,4'-COOH-2,2'-bpy)$_2$(NCS)$_2$] in Water Solution: Influence of the pH. *Chem. Phys. Lett.* 2004, 389, 204−208.

(31) Guillemoles, J.-F.; Barone, V.; Joubert, L.; Adamo, C. A Theoretical Investigation of the Ground and Excited States of Selected Ru and Os Polypyridyl Molecular Dyes. *J. Phys. Chem. A* 2002, 106, 11354−11360.

(32) De Angelis, F.; Vitillaro, G.; Kavan, L.; Nazeeruddin, M. K.; Grätzel, M. Modeling Ruthenium-Dye-Sensitized TiO2 Surfaces Exposing the (001) or (101) Faces: A First-Principles Investigation. *J. Phys. Chem. C* 2012, 116, 18124−18131.

(33) De Angelis, F.; Fantacci, S.; Mosconi, E.; Nazeeruddin, M. K.; Grätzel, M. Absorption Spectra and Excited State Energy Levels of the N719 Dye on TiO2 in Dye-Sensitized Solar Cell Models. *J. Phys. Chem. C* 2011, 115, 8825−8831.

(34) Srimath Kandada, A. R.; Fantacci, S.; Guarnera, S.; Polli, D.; Lanzani, G.; De Angelis, F.; Petrozza, A. Role of Hot Singlet Excited States in Charge Generation at the Black Dye/TiO2 Interface. *ACS Appl. Mater. Interfaces* 2013, 5, 4334−4339.

(35) De Angelis, F.; Fantacci, S.; Selloni, A.; Nazeeruddin, M. K.; Grätzel, M. Time-Dependent Density Functional Theory Investigations on the Excited States of Ru(II)-Dye-Sensitized TiO2 Nanoparticles: The Role of Sensitizer Protonation. *J. Am. Chem. Soc.* 2007, 129, 14156−14157.

(36) De Angelis, F.; Fantacci, S.; Selloni, A.; Grätzel, M.; Nazeeruddin, M. K. Influence of the Sensitizer Adsorption Mode on the Open-Circuit Potential of Dye-Sensitized Solar Cells. *Nano Lett.* 2007, 7, 3189−3195.

(37) Baková, R.; Chergui, M.; Daniel, C.; Vlček, A., Jr.; Záliš, S. Relativistic Effects in Spectroscopy and Photophysics of Heavy-Metal Complexes Illustrated by Spin−Orbit Calculations of [Re(imidazole)-(CO)$_3$(phen)]$^+$. *Coord. Chem. Rev.* 2011, 255, 975−989.

(38) Marian, C. M. Spin−Orbit Coupling and Intersystem Crossing in Molecules. *Wiley Interdiscip. Rev.: Comput. Mol. Sci.* 2012, 2, 187−203.

(39) Belpassi, L.; Storchi, L.; Quiney, H. M.; Tarantelli, F. Recent advances and perspectives in four-component Dirac−Kohn−Sham calculations. *Phys. Chem. Chem. Phys.* 2011, 13, 12368−12394.

J

dx.doi.org/10.1021/jp500869r | *J. Phys. Chem. C* XXXX, XXX, XXX−XXX

(40) Snijders, J. G.; Baerends, E. J.; Ros, P. A Perturbation Theory Approach to Relativistic Calculations. *Mol. Phys.* **1979**, *38*, 1909−1929.

(41) van Lenthe, E.; Baerends, E. J.; Snijders, J. G. Relativistic Regular Two-Component Hamiltonians. *J. Chem. Phys.* **1993**, *99*, 4597−4610.

(42) van Lenthe, E.; Snijders, J. G.; Baerends, E. J. The Zero-Order Regular Approximation for Relativistic Effects: The Effect of Spin-Orbit Coupling in Closed Shell Molecules. *J. Chem. Phys.* **1996**, *105*, 6505−6516.

(43) Visscher, L.; van Lenthe, E. On the Distinction Between Scalar and Spin-Orbit Relativistic Effects. *Chem. Phys. Lett.* **1999**, *306*, 357−365.

(44) Dyall, K. G.; van Lenthe, E. Relativistic Regular Approximations Revisited: An Infinite-Order Relativistic Approximation. *J. Chem. Phys.* **1999**, *111*, 1366−1372.

(45) Wang, F.; Ziegler, T.; van Lenthe, E.; van Gisbergen, S.; Baerends, E. J. The Calculation of Excitation Energies Based on the Relativistic Two-Component Zeroth-Order Regular Approximation and Time-Dependent Density-Functional with Full Use of Symmetry. *J. Chem. Phys.* **2005**, *122*, 204103.

(46) Wang, F.; Ziegler, T. Theoretical Study of the Electronic Spectra of Square-Planar Platinum(II) Complexes Based on the Two-Component Relativistic Time-Dependent Density-Functional Theory. *J. Chem. Phys.* **2005**, *123*, 194102−.

(47) Wang, F.; Ziegler, T. A Simplified Relativistic Time-Dependent Density-Functional Theory Formalism for the Calculations of Excitation Energies Including Spin-Orbit Coupling Effect. *J. Chem. Phys.* **2005**, *123*, 154102.

(48) Biner, M.; Buergi, H. B.; Ludi, A.; Roehr, C. Crystal and Molecular Structures of $[Ru(bpy)_3](PF_6)_3$ and $[Ru(bpy)_3](PF_6)_2$ at 105 K. *J. Am. Chem. Soc.* **1992**, *114*, 5197−5203.

(49) Damrauer, N. H.; Cerullo, G.; Yeh, A.; Boussie, T. R.; Shank, C. V.; McCusker, J. K. Femtosecond Dynamics of Excited-State Evolution in $[Ru(bpy)_3]^{2+}$. *Science* **1997**, *275*, 54−57.

(50) Felix, F.; Ferguson, J.; Guedel, H. U.; Ludi, A. The Electronic Spectrum of Tris(2,2′-bipyridine)ruthenium(2+). *J. Am. Chem. Soc.* **1980**, *102*, 4096−4102.

(51) Juris, A.; Balzani, V.; Barigelletti, F.; Campagna, S.; Belser, P.; von Zelewsky, A. Ru(II) Polypyridine Complexes: Photophysics, Photochemistry, Eletrochemistry, and Chemiluminescence. *Coord. Chem. Rev.* **1988**, *84*, 85−277.

(52) Kalyanasundaram, K. *Photochemistry of Polypyridine and Porphyrin Complexes*. Academic Press: London, 1991.

(53) Kober, E. M.; Meyer, T. J. Concerning the Absorption Spectra of the Ions M(bpy)₃²⁺ (M = Fe, Ru, Os; bpy = 2,2′-bipyridine). *Inorg. Chem.* **1982**, *21*, 3967−3977.

(54) Kumaresan, D.; Shankar, K.; Vaidya, S.; Schmehl, R. H. Photochemistry and Photophysics of Coordination Compounds: Osmium. *Top. Curr. Chem.* **2007**, *281*, 101−142.

(55) Shaw, G. B.; Brown, C. L.; Papanikolas, J. M. Investigation of Interligand Electron Transfer in Polypyridyl Complexes of Os(II) Using Femtosecond Polarization Anisotropy Methods: Examination of Os(bpy)₃²⁺ and Os(bpy)₂(mab)²⁺. *J. Phys. Chem. A* **2002**, *106*, 1483−1495.

(56) Crosby, G. A.; Demas, J. N. Quantum Efficiencies on Transition Metal Complexes. II. Charge-Transfer Luminescence. *J. Am. Chem. Soc.* **1971**, *93*, 2841−2847.

(57) Crosby, G. A. Spectroscopic Investigations of Excited States of Transition-Metal Complexes. *Acc. Chem. Res.* **1975**, *8*, 231−238.

(58) Hager, G. D.; Crosby, G. A. Charge-Transfer Excited States of Ruthenium(II) Complexes. I. Quantum Yield and Decay Measurements. *J. Am. Chem. Soc.* **1975**, *97*, 7031−7037.

(59) Hipps, K. W.; Crosby, G. A. Charge-Transfer Excited States of Ruthenium(II) Complexes. III. Electron-Ion Coupling Model for dπ* Configurations. *J. Am. Chem. Soc.* **1975**, *97*, 7042−7048.

(60) Lacky, D. E.; Pankuch, B. J.; Crosby, G. A. Charge-Transfer Excited States of Osmium(II) Complexes. II. Quantum-Yield and Decay-Time Measurements. *J. Phys. Chem.* **1980**, *84*, 2068−2074.

(61) Pankuch, B. J.; Lacky, D. E.; Crosby, G. A. Charge-Transfer Excited States of Osmium(II) Complexes. I. Assignment of the Visible Absorption Bands. *J. Phys. Chem.* **1980**, *84*, 2061−2067.

(62) Decurtins, S.; Felix, F.; Ferguson, J.; Guedel, H. U.; Ludi, A. The Electronic Spectrum of Fe(bpy)₃²⁺ and Os(bpy)₃²⁺. *J. Am. Chem. Soc.* **1980**, *102*, 4102−4106.

(63) Felix, F.; Ferguson, J.; Güdel, H. U.; Ludi, A. Electronic Spectra of M(bipy)₃²⁺ Complex Ions (M = Fe, Ru and Os). *Chem. Phys. Lett.* **1979**, *62*, 153−157.

(64) Ferguson, J.; Herren, F. The Electronic Structure of the Metal-to-Ligand Charge-Transfer States of M(bpy)₃²⁺ (M = Fe, Ru, Os). *Chem. Phys. Lett.* **1982**, *89*, 371−375.

(65) Ferguson, J.; Herren, F. A Model for the Interpretation of the Electronic Spectra of the Complex Ions M(bpy)₃²⁺ (M = Fe, Ru, Os) in D_3 and C_2 Sites. *Chem. Phys.* **1983**, *76*, 45−59.

(66) Ferguson, J.; Herren, F.; Krausz, E. R.; Maeder, M.; Vrbancich, J. Electronic Spectroscopy of M(bpy)₃²⁺ (M = Fe, Ru, Os), Cr(bpy)₃³⁺ and Related Compounds. *Coord. Chem. Rev.* **1985**, *64*, 21−39.

(67) Sauvage, J. P.; Collin, J. P.; Chambron, J. C.; Guillerez, S.; Coudret, C.; Balzani, V.; Barigelletti, F.; De Cola, L.; Flamigni, L. Ruthenium(II) and Osmium(II) Bis(terpyridine) Complexes in Covalently-Linked Multicomponent Systems: Synthesis, Electrochemical Behavior, Absorption Spectra, and Photochemical and Photophysical Properties. *Chem. Rev. (Washington, DC, U.S.)* **1994**, *94*, 993−1019.

(68) Shaw, G. B.; Styers-Barnett, D. J.; Gannon, E. Z.; Granger, J. C.; Papanikolas, J. M. Interligand Electron Transfer Dynamics in $[Os(bpy)_3]^{2+}$: Exploring the Excited State Potential Surfaces with Femtosecond Spectroscopy. *J. Phys. Chem. A* **2004**, *108*, 4998−5006.

(69) Daul, C.; Baerends, E. J.; Vernooijs, P. A Density Functional Study of the MLCT States of $[Ru(bpy)_3]^{2+}$ in D_3 Symmetry. *Inorg. Chem.* **1994**, *33*, 3538−3543.

(70) Heully, J.-L.; Alary, F.; Boggio-Pasqua, M. Spin-Orbit Effects on the Photophysical Properties of Ru(bpy)₃²⁺. *J. Chem. Phys.* **2009**, *131*, 184308−9.

(71) Lord, R. L.; Allard, M. M.; Thomas, R. A.; Odongo, O. S.; Schlegel, H. B.; Chen, Y.-J.; Endicott, J. F. Computational Modeling of the Triplet Metal-to-Ligand Charge-Transfer Excited-State Structures of Mono-Bipyridine−Ruthenium(II) Complexes and Comparisons to Their 77 K Emission Band Shapes. *Inorg. Chem.* **2013**, *52*, 1185−1198.

(72) Yersin, H.; Gallhuber, E.; Hensler, G. Highly Resolved Polarized Absorption Spectra of Single-Crystal $[Ru(bpy)_3](PF_6)_2$. *Chem. Phys. Lett.* **1987**, *134*, 497−501.

(73) Yersin, H.; Humbs, W.; Strasser, J. Low-Lying Electronic States of $[Rh(bpy)_3]^{3+}$, $[Pt(bpy)_2]^{2+}$, and $[Ru(bpy)_3]^{2+}$. A Comparative Study Based on Highly Resolved and Time-Resolved Spectra. *Coord. Chem. Rev.* **1997**, *159*, 325−358.

(74) Constable, E. C.; Raithby, P. R.; Smit, D. N. The X-Ray Crystal Structure of Tris (2,2′-bipyridine)osmium(II)hexafluorophosphate. *Polyhedron* **1989**, *8* (3), 367−369.

(75) Sauvé, G.; Cass, M. E.; Coia, G.; Doig, S. J.; Lauermann, I.; Pomykal, K. E.; Lewis, N. S. Dye Sensitization of Nanocrystalline Titanium Dioxide with Osmium and Ruthenium Polypyridyl Complexes. *J. Phys. Chem. B* **2000**, *104*, 6821−6836.

(76) Kuciauskas, D.; Freund, M. S.; Gray, H. B.; Winkler, J. R.; Lewis, N. S. Electron Transfer Dynamics in Nanocrystalline Titanium Dioxide Solar Cells Sensitized with Ruthenium or Osmium Polypyridyl Complexes. *J. Phys. Chem. B* **2000**, *105*, 392−403.

(77) Yamaguchi, T.; Miyabe, T.; Ono, T.; Arakawa, H. Synthesis of Novel β-diketonate bis(bipyridyl) Os(II) Dyes for Utilization of Infrared Light in Dye-Sensitized Solar Cells. *Chem. Commun.* **2010**, *46*, 5802−5804.

(78) *ADF2013 SCM, Theoretical Chemistry*; Vrije Universiteit: Amsterdam, The Netherlands; http://www.scm.com.

(79) te Velde, G.; Bickelhaupt, F. M.; Baerends, E. J.; Fonseca Guerra, C.; van Gisbergen, S. J. A.; Snijders, J. G.; Ziegler, T. Chemistry with ADF. *J. Comput. Chem.* **2001**, *22*, 931−967.

(80) Fonseca Guerra, C.; Snijders, J. G.; te Velde, G.; Baerends, E. J. Towards an Order-*N* DFT Method. *Theor. Chem. Acc.* **1998**, *99*, 391−403.

(81) Vosko, S. H.; Wilk, L.; Nusair, M. Accurate Spin-Dependent Electron Liquid Correlation Energies for Local Spin Density Calculations: A Critical Analysis. *Can. J. Phys.* **1980**, *58*, 1200−1211.

(82) Becke, A. D. Density-Functional Exchange-Energy Approximation with Correct Asymptotic Behavior. *Phys. Rev. A* **1988**, *38*, 3098−3100.

(83) Perdew, J. P. Density-Functional Approximation for the Correlation Energy of the Inhomogeneous Electron Gas. *Phys. Rev. B* **1986**, *33*, 8822−8824.

(84) Van Lenthe, E.; Baerends, E. J. Optimized Slater-Type Basis Sets for the Elements 1−118. *J. Comput. Chem.* **2003**, *24*, 1142−1156.

(85) van Lenthe, E.; Baerends, E. J.; Snijders, J. G. Relativistic Total Energy Using Regular Approximations. *J. Chem. Phys.* **1994**, *101*, 9783−9792.

(86) van Lenthe, E.; Ehlers, A.; Baerends, E.-J. Geometry Optimizations in the Zero Order Regular Approximation for Relativistic Effects. *J. Chem. Phys.* **1999**, *110*, 8943−8953.

(87) Stephens, P. J.; Devlin, F. J.; Chabalowski, C. F.; Frisch, M. J. Ab Initio Calculation of Vibrational Absorption and Circular Dichroism Spectra Using Density Functional Force Fields. *J. Phys. Chem.* **1994**, *98*, 11623−11627.

(88) McClure, D. S. Spin-Orbit Interaction in Aromatic Molecules. *J. Chem. Phys.* **1952**, *20*, 682−686.

(89) Klamt, A. Conductor-Like Screening Model for Real Solvents: A New Approach to the Quantitative Calculation of Solvation Phenomena. *J. Phys. Chem.* **1995**, *99*, 2224−2235.

(90) Klamt, A.; Jonas, V. Treatment of the Outlying Charge in Continuum Solvation Models. *J. Chem. Phys.* **1996**, *105*, 9972−9981.

(91) Klamt, A.; Schüürmann, G. COSMO: A New Approach to Dielectric Screening in Solvents with Explicit Expressions for the Screening Energy and Its Gradient. *J. Chem. Soc., Perkin Trans.* **1993**, *2*, 799−805.

(92) Pye, C. C.; Ziegler, T. An Implementation of the Conductor-Like Screening Model of Solvation Within the Amsterdam Density Functional Package. *Theor. Chem. Acc.* **1999**, *101*, 396−408.

(93) Monat, J. E.; Rodriguez, J. H.; McCusker, J. K. Ground- and Excited-State Electronic Structures of the Solar Cell Sensitizer Bis(4,4′-dicarboxylato-2,2′-bipyridine)bis(isothiocyanato)ruthenium-(II). *J. Phys. Chem. A* **2002**, *106*, 7399−7406.

(94) Pizzoli, G.; Lobello, M. G.; Carlotti, B.; Elisei, F.; Nazeeruddin, M. K.; Vitillaro, G.; De Angelis, F. Acid−Base Properties of the N3 Ruthenium(II) Solar Cell Sensitizer: A Combined Experimental and Computational Analysis. *Dalton Trans.* **2012**, *41*, 11841−11848.